



Euler-Equation-Based Drag Minimization of Unconventional Aircraft Configurations

Hugo Gagnon* and David W. Zingg†

University of Toronto, Toronto, Ontario M3H 5T6, Canada

DOI: 10.2514/1.C033591

This study investigates the potential of unconventional aircraft transports through numerical optimization. Three distinct configurations are investigated: a box wing, a C-tip blended wing-body, and a braced wing. Each transport is sized for the same regional mission and is subjected to the same optimization strategy based on the Euler equations. The figure of merit is inviscid pressure drag at transonic speed; the nonlinear constraints are lift, pitching moment, and internal volume. The design variables include the section shape and twist distribution of the main lifting surfaces. It is found that the box-wing, C-tip blended-wing-body, and braced-wing configurations investigated here are, respectively, 34.1, 36.2, and 40.3% more efficient than a similarly optimized conventional tube-and-wing configuration. Each optimization revealed, in one way or another, the importance of accounting for flow nonlinearity during the early stages of unconventional aircraft design. For the blended wing-body, the C tip does not appear to provide a drag benefit over a purely vertical winglet, presumably as a result of the compressibility effects prevalent in the C opening. For the braced wing, compressibility effects also lead to a curious result, where the supporting strut finds itself carrying negative lift at the optimum.

Nomenclature

b	=	span, m
C_p	=	pressure coefficient
D	=	drag, N
e	=	span efficiency
L	=	lift, N
n	=	normal force (section), m
q_∞	=	freestream dynamic pressure, N/m ²
W	=	weight, N
x, y, z	=	chordwise, spanwise, and vertical coordinates, m
α	=	angle of attack, deg

I. Introduction

FUEL economy is, now more than ever, of paramount importance for the aeronautical industry [1]. Not only do fuel-efficient aircraft cost less to operate, but they also produce less emissions responsible for climate change. One way to reduce fuel burn is to reduce drag, since thrust equals drag at steady flight. Current aircraft are, however, remarkably efficient; thus, step changes in drag reduction are unlikely unless radically new unconventional technologies are considered [2].

The two main drag components acting on a typical aircraft are viscous and induced drags. Induced drag, defined as the kinetic energy added to the wake per unit distance traveled, is an inviscid phenomenon experienced by lifting wings of a finite span. It constitutes roughly 40% of the total drag at cruise and up to a staggering 90% of the total drag during ascent [3]. Reducing this form of drag is therefore highly rewarding and is the motivation behind this study.

Munk [4] was the first to identify the elliptical lift distribution as the one producing the minimum induced drag among all planar wings of the same span and lift. His results were based on the well-known lifting-line theory of Prandtl [5], which was later refined by Cone [6] for lifting systems with “spanwise camber.” These and other ideas culminated in the vortex-lattice method and its use in numerical optimization to find the minimum induced drag of arbitrary nonplanar lifting systems [7].

Although nonplanar wings may produce less induced drag compared to planar wings of the same span and lift, aircraft are not built on the basis of induced drag with fixed span and lift. To account for viscosity, structures, and other effects, several authors have recently coupled their aerodynamic analyses with other models of varying degrees of fidelity; see, for example, [8–12]. Although insightful, these studies are nonetheless limited by the linear aerodynamic assumption.

van Dam [13] demonstrated that higher span efficiencies than those predicted by linear theory are possible for planar crescent-moon-shaped wings, since such wings shed a nonplanar wake at an angle of attack. Smith [14] and Smith and Kroo [15] confirmed that beneficial nonlinear wing-wake interaction can indeed lead to lower induced-drag values, provided that the shape of the rolled-up force-free wake is accurately modeled. More recently, Liersch et al. [16] concluded that higher-order effects such as induced lift explained why a spanwise cambered elliptical wing produced less induced drag than the same unfolded wing.

Another important yet often overlooked nonlinear effect influencing induced drag is compressibility. Even with the Prandtl–Glauert correction, incompressible-flow models at higher Mach numbers fail to predict the correct optimal lift distribution of simple planar objects such as sweptback wings [14]. For nonplanar wings in transonic flow, the incompressible assumption is not only inaccurate but also unreliable.

The necessity of incorporating high-fidelity models in the investigation and assessment of unconventional aircraft is being increasingly recognized [17–19]. The difficulty, of course, is to use such models effectively as design tools. In the case of models based on computational fluid dynamics (CFD), aerodynamic shape optimization (ASO) is invaluable, since it has the potential to exploit the nonlinearity of the flow without human intervention beyond problem setup [20].

Applications of CFD-based ASO to wing design have, up until recently, largely focused on the Euler equations [21–28]. Contrary to circulation-distribution and panel methods, the Euler equations do not require the user to prescribe the starting location and shape of the wake. Compressibility effects are also inherently captured. On the

Received 13 June 2015; revision received 24 November 2015; accepted for publication 12 January 2016; published online 10 May 2016. Copyright © 2016 by Hugo Gagnon and David W. Zingg. Published by the American Institute of Aeronautics and Astronautics, Inc., with permission. Copies of this paper may be made for personal and internal use, on condition that the copier pay the per-copy fee to the Copyright Clearance Center (CCC). All requests for copying and permission to reprint should be submitted to CCC at www.copyright.com; employ the ISSN 0021-8669 (print) or 1533-3868 (online) to initiate your request.

*Ph.D. Candidate, Institute for Aerospace Studies, currently Development Engineer, NUMECA International, Chaussée de la Hulpe 189, 1170 Brussels, Belgium. Student Member AIAA.

†Professor and Director, Institute for Aerospace Studies, Tier 1 Canada Research Chair in Computational Aerodynamics and Environmentally Friendly Aircraft Design, J. Armand Bombardier Foundation Chair in Aerospace Flight. Associate Fellow AIAA.

downside, the influence of viscosity on induced drag is ignored; in particular, side-edge flow separation at the wingtips may not match the true viscous flow [14].

This study uses ASO based on the Euler equations to investigate the potential for induced-drag reduction of four transonic aircraft configurations. Consistency is emphasized; each configuration is sized for the same mission and is optimized using the same geometry control system as well as the same flow solver and optimizer. Stability, structures, and other such considerations are purposefully excluded from the analyses so as to isolate the role of flow nonlinearity on induced drag.

This study does not attempt to provide a definite answer as to which unconventional aircraft configuration is superior to the other, nor does it attempt to find the “real-world” optimum for each configuration. Such questions can only be answered through multidisciplinary, multiobjective, and multipoint optimizations involving high-fidelity viscous flow models. Instead, this study focuses on the influence of flow nonlinearity on the aerodynamic design and induced drag of unconventional aircraft.

Section II of this paper describes the methodology used to carry the optimizations. Specifically, Sec. II.A reviews each aircraft configuration in the context of previous work, Sec. II.B overviews the optimization problem common to all four configurations, and Sec. II.C gives some details on the grids used throughout the optimizations. The results of those optimizations are presented in Sec. III, where Secs. III.A to III.D are each assigned one configuration. Finally, Sec. IV summarizes the main findings and concludes the paper.

II. Methodology

A. Concept Selection

Many unconventional aircraft transports have been proposed throughout the history of aviation. Each transport represents a compromise between competing objectives and constraints for a given mission. Lange [29], for example, reviewed a flatbed, a multibody, and a wing-in-ground-effect configuration for very large cargo aircraft.

The configurations investigated here are targeted at the medium-haul 100-passenger market segment. They are a tube and wing, a box wing, a C-tip blended wing-body, and a braced wing. Relative to the tube and wing, each unconventional configuration has the potential to substantially reduce induced drag. Although other configurations such as the D8 aircraft of Drela [30] are equally promising in that regard, here priority is given to those configurations with larger vertical extents for their more interesting nonplanar wake structure.

Figure 1 depicts the initial geometry of all four transports. Their planform is based on already existing designs, which are scaled for the present study to ensure that the fuselages contain enough room to house the passenger compartments (also visible in Fig. 1). Note that the fuselages and engines shown here are not included in the flow analyses of the ASO problems,[‡] although their weights are considered, as explained in Sec. II.B.

With the exception of the bracing strut in Fig. 1d, the wings of each transport are generated exclusively from NASA's integral supercritical airfoils [31]. These airfoils are characterized by a large leading-edge radius, thus providing reasonable low-speed performance, and a reduced curvature over the middle region of the upper surface, thus delaying the shock and, ultimately, drag rise. They thus provide an excellent starting point for the ASO problems since, here, the freestream Mach number is fixed at 0.78 for all cases, which is in agreement with the reported cruising speeds of most regional jet transports.

Wing segments (the darker surfaces separated by thin black lines in Fig. 1) are each generated by sweeping a root airfoil or a blend of a root and tip airfoils along a trajectory curve [32]. The airfoils are used

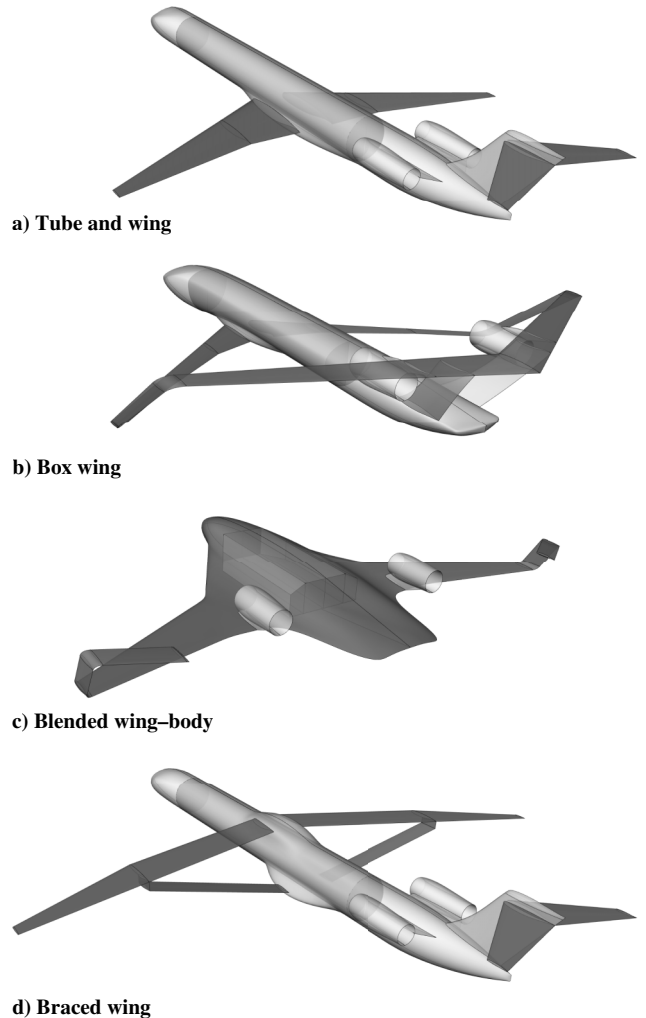


Fig. 1 Regional transports.

as is, with the exception of the centerbody of the blended wing-body, for which the thickness-to-chord ratio of the root airfoil is increased by scaling it in the vertical direction. Also, for the blended wing-body only, the blending between the root and tip airfoils is nonlinear; specifically, the blending is linear from root to midspan and then constant based on the tip airfoil only.

An overview of each transport is given next; refer to Table 1 for more detailed specifications.

1. Tube and Wing

The baseline tube and wing shown in Fig. 1a is modeled after publicly available information on the Bombardier CRJ1000.[§] The pressurized cabin is designed for a 2–2 seating arrangement and is long enough to seat 104 passengers in economy class.

The main wing is essentially a scaled-up version of the CRJ700 planform: a straight leading-edge swept back 30 deg with a root plug ending at 35% semispan. Based on a mix of historical trends and two-dimensional methods, as described by Raymer [33], the NASA SC(2)-0614, SC(2)-0412, and SC(2)-0410 airfoils are chosen at the root, kink, and tip sections, respectively. This choice yields satisfactory lift coefficients and internal volume at the expense of small wave-drag penalties.

Rather than trying to replicate the exact winglet of the CRJ1000, the choice is made to not include a winglet on the initial geometry; however, as will be discussed in Sec. III.A, the optimizer is given enough freedom to produce one on its own.

[‡]Including the fuselage alongside a wing in a shape optimization problem introduces a host of difficulties [22]; in fact, retaining the design intent (quality) of the fairing at a wing-body junction is arguably the most challenging task of any aerodynamic optimizer.

[§]Data available online at <http://commercialaircraft.bombardier.com/en/crj.html> [retrieved 1 May 2015].

Table 1 Dimensions and key data

	Tube and wing	Box wing	Blended wing-body	Braced wing
<i>Dimensions, m</i>				
Wing span	26.30	26.30	30.73	34.15
Overall length	38.79	34.31	21.10	38.79
Overall height	6.15	6.60	3.81	6.02
<i>Wetted area, m²</i>				
Wing	134.23	179.81	478.58	182.69
Fuselage	282.91	285.73	—	291.72
Horizontal tail	30.43	—	—	30.43
Vertical tail	21.10	30.76	—	21.10
Total	468.66	496.30	478.58	525.92
<i>Weight and balance^a</i>				
W/q_{∞} , m ²	38.16	39.18	40.10	39.84
Center of gravity, ^b m	4.44	10.34	12.39	4.05

^aAt the beginning of the cruise segment.^bMeasured from the leading edge of the foremost wing segment at the symmetry plane.

2. Box Wing

For a fixed span, the box wing is most appealing from the perspective of induced drag: in theory, if the two wings of a biplane are infinitely separated, and each one carries half the lift of a monoplane of the same span, then the induced drag is halved. If, further, a biplane is joined at its tips by end plates, then reductions on the order of 40% are predicted for vertical-gap-to-span ratios of about 0.3 [5]. These results should also hold for swept wings in transonic flow by virtue of Munk's stagger theorem [4].

In practice, several difficulties were uncovered in the high-subsonic regime by Lange et al. [34]. Chief among these was wing divergence encountered well below the target flutter speed. This problem was also well recognized by Frediani [35], whose solution was to mount the rear wings on two vertical fins separated by a maximum horizontal distance. Although the models employed in the present study do not account for aeroelasticity, the two fins are nevertheless positioned aft of the fuselage as shown in Fig. 1b, even though like the fuselage they are excluded from the aerodynamic analyses.

The initial airfoil selection is of little importance, since the flow curvature induced by the neighboring wings calls for highly customized airfoils [36]. Here, most of the wing loop is generated from the NASA SC(2)-0410 airfoil, with the exception of the vertical tip fins, which are generated from the NASA SC(2)-0010 symmetric airfoil.

3. Blended Wing/Body

Unlike most unconventional transports, the blended wing-body has been the subject of many ASO studies based on flow models as accurate as the Reynolds-averaged Navier–Stokes equations [37–41]. This popularity is undoubtedly due to its geometric simplicity (in its simplest form, the blended wing-body is really just a wing with nonlinearly varying taper).

The blended wing-body shown in Fig. 1c is inspired from the released press on the X-48C demonstrator. Unlike the X-48C, it features C-tip extensions, thus providing longitudinal and directional control and stability on top of mitigating induced drag [3].

The nose bullet, intended for increased cockpit visibility, somewhat complicates surface generation. Indeed, the challenging task of fitting the necessary volume inside a compact yet smooth blended wing-body of this size might very well explain its usual application to very large transports [42,43]. Here, a 2–4–2 cabin layout is assumed to ensure ride quality, with the cargo bays and fuel tanks located outboard.

An airfoil stack arising from the combination of a (modified) NASA SC(2)-0010 airfoil at the root and an (unmodified) NASA SC(2)-0410 airfoil at the tip is fitted in a single sweep to generate a C^2 continuous outer mold line. No initial twist is prescribed; therefore, the initial configuration generates barely any lift. However, as will be pointed out in Sec. III.C, the optimizer easily remedies this situation by pitching up the centerbody by only a few degrees.

4. Braced Wing

Braced wings can be traced back to the early days of aviation, but it is Pfenninger [44] who revived the concept for high-speed transports. The design motivation is to use a strut, or a system of trusses, to alleviate wing bending–torsion. This in turn allows for higher aspect-ratio wings with lower thickness-to-chord ratios. The thinner wings have less transonic wave drag, permitting the wings to unsweep, thus favoring natural laminar flow.

Understandably, aerostructural considerations are particularly important in the design of braced wings. Elements of multidisciplinary analysis and optimization have thus been incorporated in recent studies [45–50]. Although some of these studies involve CFD, none involve CFD-based ASO.

As per the general guidelines of Bhatia et al. [48], the strut of the braced wing shown in Fig. 1d intersects the wing at a 60% semispan. The span is chosen to be 1.3 times that of the tube and wing, leading to an aspect ratio of roughly 16.4; in comparison, values of 16.0, 16.4, and 19.55 are reported in [50], [44], and [49], respectively. As in [50], the strut is unswept and, as in [45], it has a vertical portion aimed at reducing compressibility effects at the wing–strut junction.

The wing is generated from the NASA SC(2)-0412 airfoil at the root and the NASA SC(2)-0410 airfoil at the tip, whereas the strut is entirely generated from the NACA 64A-010 symmetric airfoil. Just like the previous three transports, all wing segments are initially untwisted, and those intersecting the fuselage (i.e., the symmetry plane) have zero angle of incidence.

B. Optimization Problem

To draw direct comparisons based on absolute drag, it is important that all four transports be optimized in a consistent manner. To begin with, each transport must be able to perform the same mission, which consists of carrying 100 passengers and three crew members over 926 km (≈ 550 miles) at Mach 0.78 and an altitude of 10.5 km ($\approx 35,000$ ft). Since only single-point optimizations are conducted here, the most critical point of the cruise segment is picked i.e., at the beginning, where the required lift is maximum.

As stated in Sec. I, real-world applications normally require multiple flight conditions to be included within the same optimization problem. The main building blocks of the optimizer are described and validated in [51]. Multipoint optimizations are, however, beyond the scope of this work (as are structural deflections and other important effects). Here, the focus is on nonlinear aerodynamics not easily captured with panel or other simplified methods.

For each case, the sum of induced and wave drags (i.e., inviscid pressure drag) is minimized using the same gradient-based aerodynamic optimizer. The main building blocks of the optimizer were described and validated by Hicken and Zingg [51]. In particular, it solves the Euler equations on multiblock structured grids and computes the gradients of the flow-dependent functionals using the discrete-adjoint method.

Surface deformation is handled by a geometry control system based on two-level free-form and axial deformation [52]. Using this technique, so-called axial curves handle variations in sweep, span, and dihedral, while free-form-deformation (FFD) volumes handle variations in twist, taper, and section shape. Both the axial curves and the FFD volumes are modeled with B splines.

As shown in Fig. 2, in general one axial curve is used per wing segment, irrespective of its length and function. Doing so allows one to retain the design intent of the wing systems, as opposed to using a single continuous axial curve to parameterize, for example, the entire box wing. This approach also greatly simplifies problem setup, since the trajectory curves used to generate the wing segments can then be reused as axial curves. Note that only the end control points of the axial curves are shown in Fig. 2, except for the top wing of the box wing, for which the middle control point is also shown.

Some of the axial-curve control-point coordinates are activated with the goal of exploring the design space of each configuration. Depending on the configuration at hand, an attempt is made to do so in a manner that is sensible both from an aerodynamic and a structural



To prevent the wings from becoming excessively thin as a result of the optimizations, their internal volume is forced to maintain at least 95% of their initial value. Additionally, the vertical scaling factors responsible for section shape control are constrained to a lower bound of 0.6. Thus, for example, a wing section that is initially 10% thick cannot become less than 6% thick. This is with the exception of the cross sections covering the centerbody of the blended wing-body, for which, given the cabin height requirement, the lower bound is set to 0.95.

Note that the aircraft weights are used for the sole purpose of calculating the target lift at the beginning of each optimization. During the optimizations, the effect of varying twist and section shape on the surface area, and therefore the weight, is not accounted for. Even if it were, the variations in weight would be small, since, as discussed in the previous paragraphs, the design parameters responsible for span, sweep, and taper are, in general, fixed. The lower bounds on section shape control and the internal volume constraint further limit variations in wetted areas.

Table 2 Grid data in root-chord units

		Spacing ($\times 10^{-3}$)		Far-field distance ^a	
Block	Node	Offwall	Wall ^b		
<i>Tube and wing</i>					
Coarse	126	3 466 800	0.0989	11.60	25.0
Fine	2544	97 712 968	0.0278	3.83	25.0
<i>Box wing</i>					
Coarse	96	3 395 562	0.3524	15.30	24.4
Fine	2354	98 001 819	0.1021	4.99	24.4
<i>Blended wing-body</i>					
Coarse	234	1 540 000	0.2459	5.74	25.0
Fine	2391	91 652 311	0.0434	1.47	25.0
<i>Braced wing</i>					
Coarse	248	4 436 424	0.3107	27.74	20.9
Fine	2191	95 023 706	0.1170	10.06	20.9

^aAverage surface spacing $\equiv \sqrt{S/N_{\text{surf}}}$, where S is the surface area and N_{surf} is the number of nodes on the surface.

^bMinimum distance to the far-field boundary.

The center of gravity of the tube and wing is set at 25% of its mean aerodynamic chord (MAC), whereas the centers of gravity of the unconventional aircraft are calculated based on their component-weighted centroids. The longitudinal position of the centers of gravity is considered a design variable, with an upper bound of 35% MAC for the tube and wing. For the unconventional aircraft, a margin of 5% of the fuselage length is used in order to account for their greater uncertainty in wing planform and overall design.

C. Baseline Grids

Predicting drag through CFD in the context of ASO is not without difficulty. Not only does artificial dissipation affect the solution but, also, the thin shape of wings makes it difficult to accurately resolve pressure gradients with reasonable mesh sizes [53]. Even though wake-plane analyses are typically more accurate than surface-based predictions [54], this trend diminishes with increasing mesh density [23]. The approach taken here, therefore, is to use coarse grids to run the optimizations and to use fine grids to retrieve grid-converged lift and drag values, either before or after the optimizations have taken place. Based on the authors' experience, see also [55], this approach yields similar relative results compared to optimizations conducted on finer grids, even though the absolute drag values can differ significantly on the finer grids. Of course, using coarse grids for the optimizations has the added benefit of significantly reducing computational cost. A breakdown of the CPU time required to evaluate the objective function and gradient components on grids comprising millions of nodes is given in [51].

Some statistics of the baseline grids are listed in Table 2. The final spacings will vary slightly as a result of mesh movement. However, the offwall spacings at the wing roots will remain on the order of 10^{-3} root-chord units. The fine grids are obtained by refining, in parameter space, the B-spline block mappings responsible for mesh movement [51], thus ensuring that the surface nodes coincide with the underlying geometry. The refined grids are used to produce all the plots and figures of Sec. III.

The smaller offwall spacings of the tube and wing relative to the other configurations are due to the wingtip treatment. Node clustering is used to ensure that the optimizer catches the right (subtle) aerodynamic tradeoffs when morphing a winglet. Also, taper is applied to the baseline surface grid at the tip, which further reduces the mesh cell sizes there by a factor of three or so.

III. Results

The results of the drag minimizations summarized in Table 3 are now discussed for each configuration. Since lift and span are constrained in all cases, the drag minimizations are equivalent to span-efficiency maximizations. Recall that the span efficiency of a lifting system can be computed without resorting to reference areas:

Table 3 Summary of the drag minimizations

	e	L/D	$L/q_{\infty}, \text{m}^2$	$D/q_{\infty}, \text{m}^2$
Tube and wing	1.026	54.3	40.71	0.7491
Box wing	1.479	80.3	39.69	0.4939 (−34.1%)
Blended wing-body	1.207	86.1	41.20	0.4782 (−36.2%)
Braced wing	0.993	89.9	40.22	0.4472 (−40.3%)

$$e = \frac{(L/q_{\infty})^2}{\pi b^2 (D/q_{\infty})} \quad (1)$$

Recall also that this metric is only relevant for lifting systems of the same span and lift; therefore, although it provides a useful benchmark against linear theory, it is not intended to compare the relative performance of the configurations.

As described in Sec. II.B, the analyses do not account for viscous drag, and the optimizations do not include the fuselage, engines, and vertical tail of the configurations. It is therefore important to take the L/D , and thus the percentage improvements, in this context. The wetted areas are, however, more or less the same before and after the optimizations as a result of fixing span, sweep, and taper, which also prevent the optimizer from exploiting the planform shapes in favor of even lower inviscid drag values.

Euler-equation-based solutions are often characterized by unrealistic pressure recovery regions due to the inability of the Euler equations to model flow separation [56]. Despite this limitation, the pressure-coefficient and wing profiles of each configuration are still reported in this section. The intent is to give the reader insight into the physics as opposed to suggesting what the profiles should look like on real aircraft.

The values reported in Table 3 are computed from post-optimization fine-grid flow analyses. Consequently, the lift values reported here differ from the target lift values used for the optimizations. This can be seen by comparing the W/q_{∞} and L/q_{∞} values in Tables 1 and 3, respectively. Had the angles of attack been adjusted at the end of the optimizations to recover the target lift values, the drag values would be more or less 6% lower (since the lift values are on average 3% larger than the target values). That being said, the absolute drag values are somewhat irrelevant; what matters here is the relative performance of the configurations as reported in the last column of Table 3. Although more work is needed, these performance trends are expected to remain the same should the weight estimates, and therefore the target lift values, change slightly (as a result of using a different weight model or optimizing at different cruise conditions, for example).

A. Tube-and-Wing Configuration

The initial tube-and-wing configuration is shown on the left-hand side of Fig. 3a. Shocks are clearly visible aft on the inboard wing and outboard close to the leading edge. To remedy this, a total of five axial curves are defined, as shown in Fig. 2a. The first four axial curves are assigned to the wing and are positioned directly on its leading edge, thus ensuring that the latter remains straight regardless of twist, whereas the fifth axial curve is positioned on the quarter-chord curve of the horizontal tail. The axial curves control a total of 23 independent FFD-volume cross sections. All cross sections are allowed to twist; however, there are only seven effective twist design variables since, for any given FFD volume, twist is linearly interpolated between the tip cross sections. Each and every control point forming the 19 cross sections controlling the wing is allowed to scale along its local vertical axis, leading to 380 section design variables (19×20). Finally, the x and z coordinates of the fourth axial curve's outermost control point can vary. The intent is to encourage the optimizer to produce a winglet on its own by controlling the streamwise and vertical extents of the wingtip extension. A smooth wing-winglet transition is ensured by the third axial curve. Note that taper is enforced manually on the winglet at the beginning of the optimization, and is therefore not a design variable.

Figure 3a on the right-hand side shows the optimized wing and tail. All shocks are eliminated and, as expected, the optimizer reached the upper bound of the winglet's streamwise and vertical extents. By reshaping the remaining wing segments, the optimizer also managed to achieve a span efficiency greater than one despite the trim constraint. This efficiency gain is reflected by the smoother structure of the wake on the right-hand side of Fig. 3b. Note that the wake structures shown in this paper are produced from views located 80 m downstream of the configurations and perpendicular to the reported angles of attack.

Compared with the initial configuration, the spanwise normal-force distribution of the optimized configuration is much more elliptical; see Fig. 4. The winglet thus experiences significant side

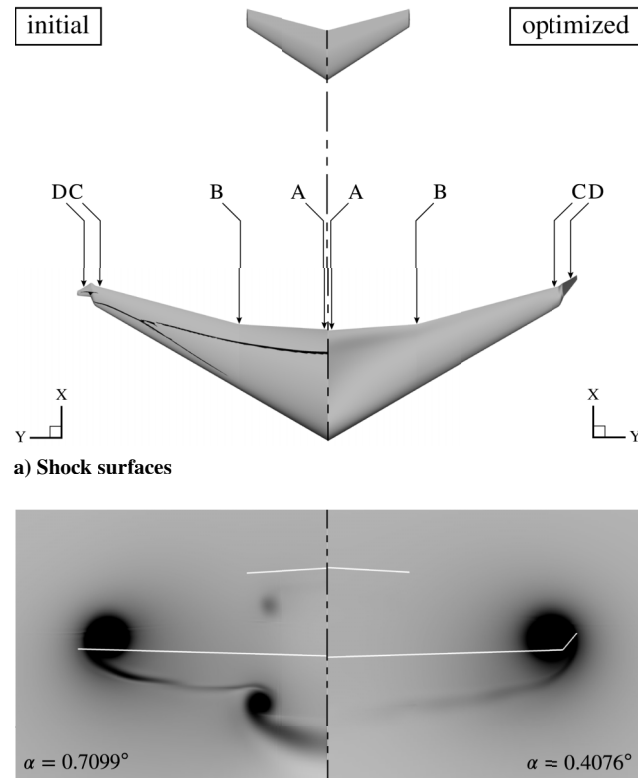


Fig. 3 Initial (left) and optimized (right) tube-and-wing configurations.

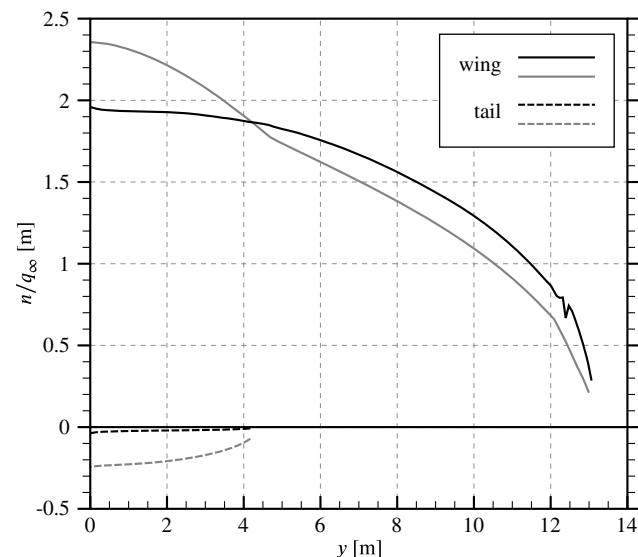


Fig. 4 Initial (gray) and optimized (black) normal-force distributions of the tube-and-wing configuration.

forces, which is in agreement with the design guidelines of Whitcomb [57]. As for the tail, it is forced to carry some negative lift due to the position of the center of gravity, which in turn forces the optimizer to increase the loading on the wing in order to achieve the required total lift while keeping the force distribution smooth. The optimizer tries to minimize this balancing act by heavily contorting the wing sections, especially at the root (section A), as seen in Fig. 5. The pressure recovery regions are nevertheless much more gentle on the optimized sections, except perhaps on the suction side of the winglet, where the steep pressure gradients would likely cause separation in viscous flow [56]. Of particular interest is the striking resemblance between section D of the optimized winglet and the "typical winglet section" reported by Whitcomb in his seminal 1976 study ([57] p. 19, figure 3).

For comparison, the same optimization problem was repeated but without the permissible vertical extent (that is, with one less degree of freedom), and it was found that the winglet-up configuration produced roughly 3.5% less drag.

B. Box-Wing Configuration

The initial flow solution of the box-wing configuration is smoother overall than that of the tube and wing due to its thinner airfoils, with the exception of a strong but thin shock located outboard along the leading edge of the front wing and a localized supersonic bubble at the leading-edge root of the rear wing; see Fig. 6a. Smooth flow gradients are also observed on the inboard portion of the vertical tip fin. To set up the optimization, one axial curve is positioned on the leading edge of each wing segment, including the two corner fillets, for a total of seven axial curves. In all, there are 26 FFD-volume cross sections, totaling 520 section design variables (26×20). Like the tube and wing, all middle cross sections of each FFD volume are linearly interpolated from the tip cross sections; thus, there are only eight effective twist design variables. Finally, the optimizer is also given some freedom in shaping the planform of the top wing through the middle control point of its axial curve (see Fig. 2b), which is quadratic. Only the x (chordwise) coordinate of that control point is allowed to vary.

By the end of the optimization, the optimizer reached the lower bound of that last design variable, leading to the nonlinear planform shape shown on the right-hand side of Fig. 6a. As seen in the same

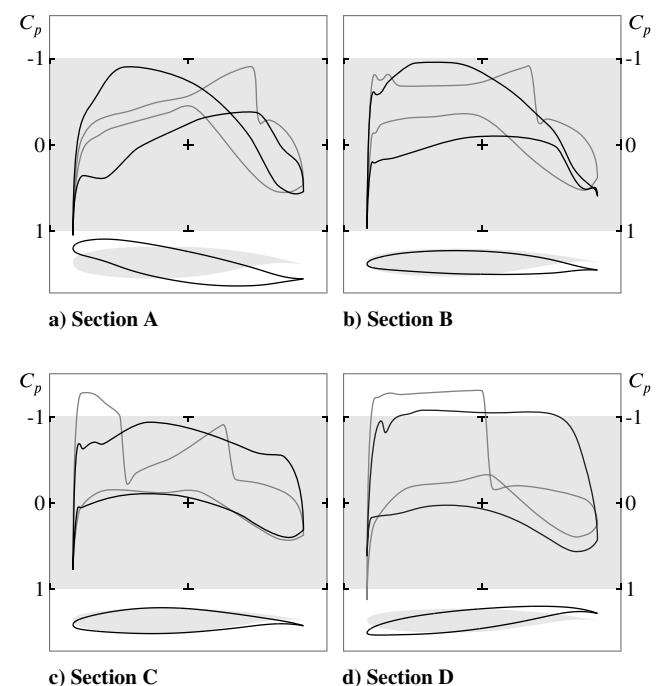


Fig. 5 Initial (gray) and optimized (black) pressure-coefficient profiles of the tube-and-wing configuration. Sections A–D correspond to those of Fig. 3a.

figure, the optimizer also removed all shocks. It also redistributed the load carried by each wing segment (see Fig. 7), resulting in smooth spanwise and vertical force distributions. The final span efficiency is 1.479; in comparison, according to Frediani [35], the span efficiency of a box wing of a height-to-span ratio of 0.2 and no dihedral should be about 1.47. The span efficiencies are thus in excellent agreement. However, it should be noted that the effective height-to-span ratio of the optimized configuration is in fact closer to 0.3 when accounting for the final angle of attack of -5° . This can be seen by comparing the height of the initial and final axial curves in Fig. 6b. Also of particular interest in Fig. 6b is the final wake structure of the

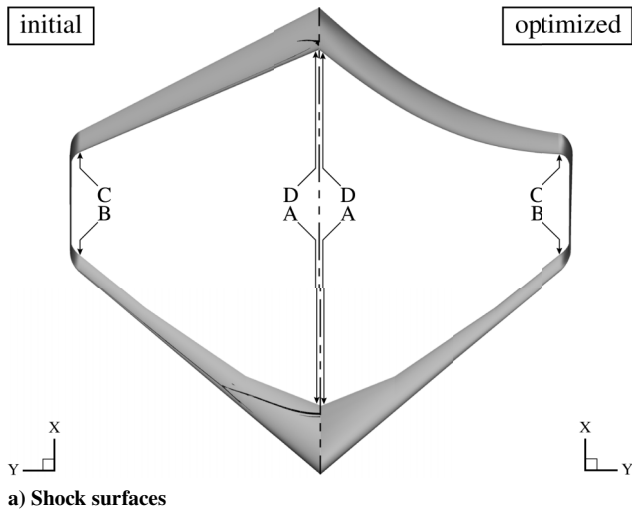
optimized configuration, which has its number of vortex cores reduced to two down from four.

By reaching the lower bound of -5° deg on the angle of attack, the optimizer effectively maximized the vertical distance between the top and bottom wings when looking toward the out-of-plane axis (i.e., the axis perpendicular to the plane passing through both wings). This is expected since, for box wings, the larger the height-to-span ratio, the larger the span efficiency [5]. To investigate the impact of the angle of attack on the solution, the same optimization was set up but without any bound on the angle of attack. Although this second optimization resulted in considerably less drag, it eventually failed at an angle of attack of about -16° deg. The failure was attributed to mesh movement problems caused by heavy twisting of the wings, which is necessary to satisfy the lift and trim constraints. Presumably, if the optimizer could, it would completely realign the freestream along the out-of-plane axis to maximize span efficiency. Although of academic interest, this solution has of course no practical value.

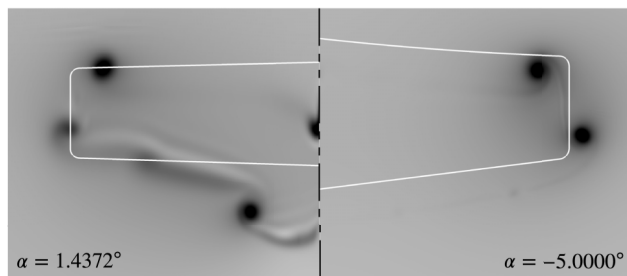
In contrast to the span efficiency, the force distributions shown in Fig. 7 may at first glance appear a little surprising. The optimal force distribution of the box wing is generally shown as the sum of a constant and elliptical lift distributions that is equally carried by the top and bottom wings, joined at their tips by butterfly-shaped side-force distributions [5]. However, as remarked by Kroo [3], what this observation does not account for is that a vortex loop of constant circulation can be superimposed on such a closed system without changing its total lift and drag. This is indeed what is observed in Fig. 7: the force distribution is similar to the one described previously, only here it is slightly “shifted” onto the top wing. Given the gradient-based nature of the optimization, this result is likely sensitive to the initial design and flow conditions, i.e., it corresponds to a local optimum.

The remarkable capability of the box wing to adapt its optimal force distribution at virtually no performance cost is confirmed in a recent study by Gagnon and Zingg [58], who also showed that, when trim, stability, and root-bending moment constraints are included in the optimization problem, then a box wing outperforms a tube and wing by 17.8% more than when no such constraints are imposed.

As seen in Fig. 8, the flowfield induced by the neighboring wings has a substantial impact on the wing sections. Similar trends to those observed on the joined wing by Wolkovitch [59] are visible. First, whereas the bottom wing is washed out (the incidence at section B is



a) Shock surfaces



b) Wake structure

Fig. 6 Initial (left) and optimized (right) box-wing configuration.

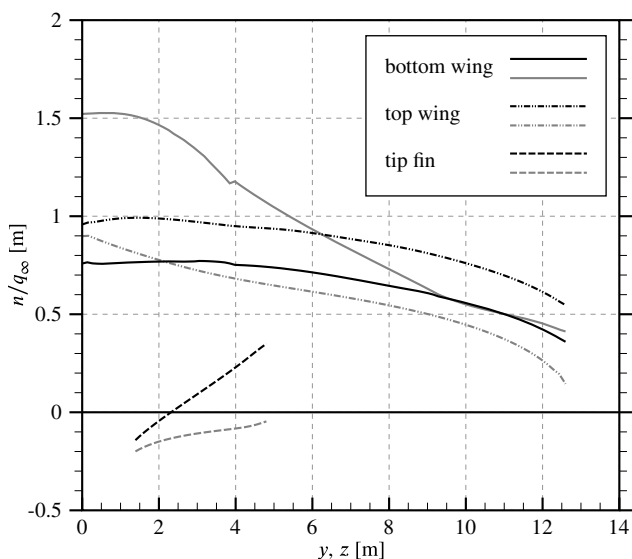


Fig. 7 Initial (gray) and optimized (black) normal-force distributions of the box-wing configuration.

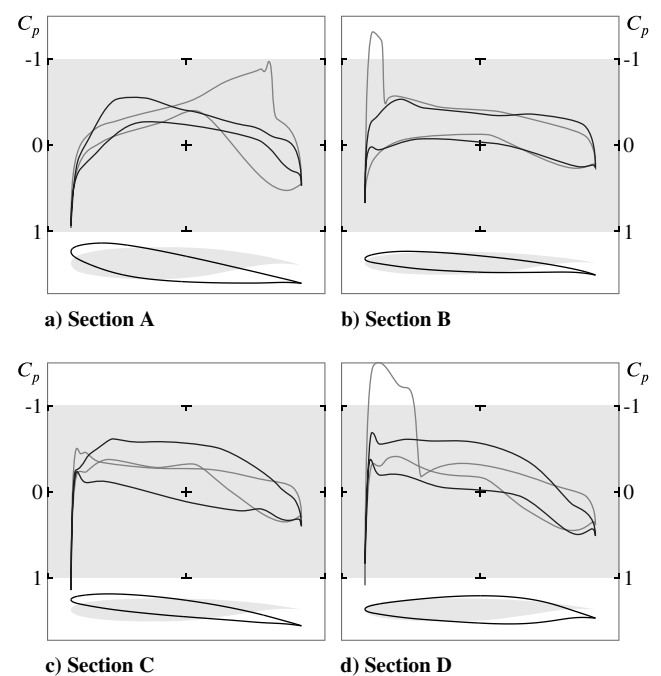


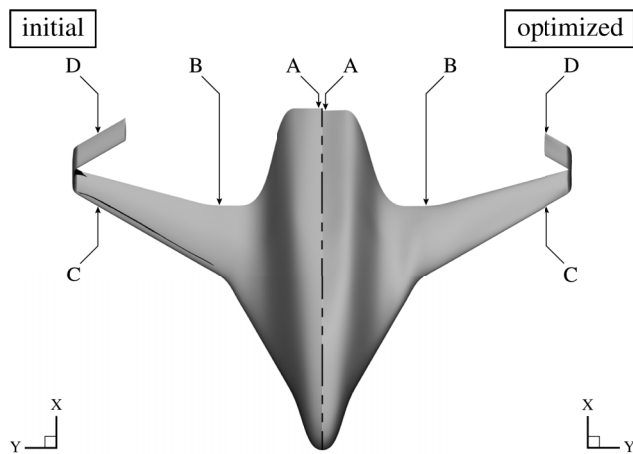
Fig. 8 Initial (gray) and optimized (black) pressure-coefficient profiles of the box-wing configuration. Sections A–D correspond to those of Fig. 6a.

less than at section A), the bottom wing is washed in (the incidence at section D is more than at section C). Second, the bottom wing (sections A–B) incorporates more camber than the bottom wing (sections C–D).

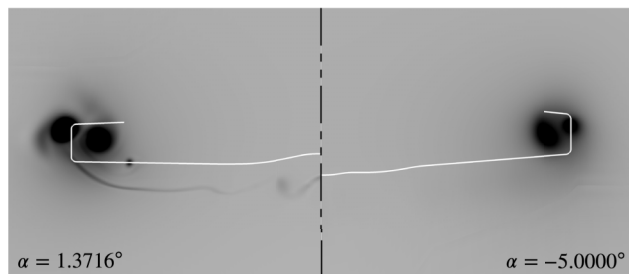
C. Blended-Wing/Body Configuration

Inspecting Fig. 9a, the initial blended-wing–body configuration has shocks, both on the outboard wing and in the transonically stressed flow environment located inside its C-tip extension. For the optimization, a total of five axial curves are used, visible in Fig. 2c: one going from the root of the centerbody all the way to the tip, one for the vertical tip fin, one for the horizontal winglet, and two for the smooth corner transitions. All the axial curves are positioned on the leading edge of their respective wing segment. There are a total of 29 FFD-volume cross sections, and section shape control is activated on each one of them, leading to 580 section design variables (29×20). Twist is linearly constrained between the root, midspan, and tip cross sections of the centerbody-outboard segment, as well as on the other wing segments between their tip cross sections, for a total of seven effective twist design variables.

The blended wing–body studied here is, in a sense, doubly unconventional with its C-tip extension. Unlike their planar counterparts, the aerodynamics of C-tip blended wing–bodies have not received much attention in the past; see [60] for a rare exception. Thus, the focus here is on the C-tip extension: more specifically, on its top horizontal segment. Originally, both its length and dihedral angle were allowed to vary, but the optimizer invariably tried to eliminate it in favor of a higher vertical winglet, i.e., it wanted to “unfold” the C shape. Another optimization was thus set up, where this time the horizontal segment could only vary in length. As seen from the resulting planform in Fig. 9a, the optimizer still chose to reduce the horizontal segment’s length as much as it could, suggesting that, for a fixed vertical-gap-to-span ratio, the C tip is not advantageous (perhaps even disadvantageous) over a purely vertical winglet. Although surprising, a similar conclusion was reached by Verstraeten



a) Shock surfaces



b) Wake structure

Fig. 9 Initial (left) and optimized (right) blended-wing–body configurations.

and Slingerland [8] when comparing optimally loaded wingletted and C wings based on total drag.

As seen in Fig. 10, the spanwise force distribution on the centerbody of the blended wing–body remains nonmonotonic after the optimization. Similar observations were made by Qin et al. [37], who attributed this result to the compressibility effects arising from the lateral disturbances caused by the presence of a highly tapered centerbody. Surprisingly, the horizontal winglet experiences a downward force at optimality, a finding that is, however, consistent with those of others [3,8,61].

Just as interestingly, as seen in Fig. 9b, the optimizer partially merged the two tip vortices, thus reducing the kinetic energy lost to the wake and therefore the induced drag. Similar to the box wing, it also maximized the vertical distance between the top and bottom wings (i.e., the effective height-to-span ratio) by reaching the lower bound of -5° deg on the angle of attack. Relative to this value, the

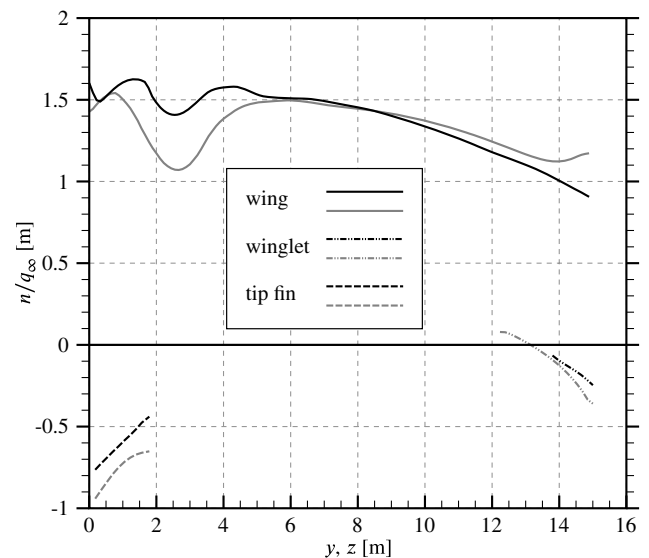


Fig. 10 Initial (gray) and optimized (black) normal-force distributions of the blended-wing–body configuration.

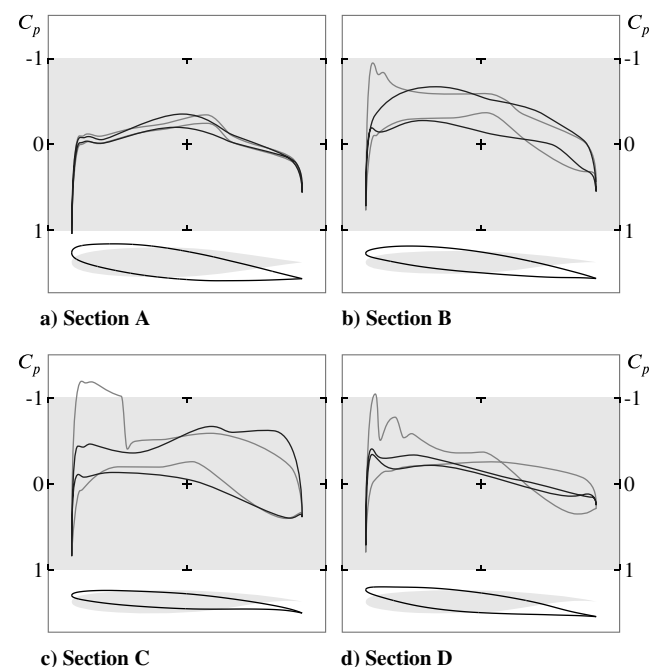


Fig. 11 Initial (gray) and optimized (black) pressure-coefficient profiles of the blended-wing–body configuration. Sections A–D correspond to those of Fig. 9a.

incidence angle of the centerbody's root section reached 2.1 deg, thus favoring a reasonable deck angle at cruise. As seen in Fig. 11, the incidence angles at the tip (sections C and D) are also small relative to the freestream and, similar to the box wing, the thickness-to-chord ratios are larger at the top (section D) than at the bottom (section C).

D. Braced-Wing Configuration

Shocks reside on most top surfaces of the initial braced wing despite its thin sections and relatively small wing loading. Axial curves are assigned to wing segments in a similar fashion as in the previous three cases, yielding five effective twist and 340 section design variables. The strut, being a purely structural member, is not allowed to twist and has limited freedom in section shape changes. The extent of its vertical portion, however, is allowed to change by plus or minus 0.1 root-chord units. The intent is to help the optimizer relieve the flow passing through the wing-strut opening. Finally, with the exception of the section located at the wing-strut junction, taper is activated on all 11 FFD-volume cross sections covering the main wing segments. Because the axial curves are positioned on the wing's trailing edge, the latter is ensured to remain straight as taper is varied.

The flow on the optimized shape is remarkably well behaved, as evidenced by the absence of shocks and the much weaker trailing vortices on the right-hand sides of Fig. 12. Notice how the initial kink at 60% semispan disappears, blended by a smooth leading edge.

Even more interesting is the fact that the span efficiency of the full system is very close to unity, despite the strut carrying a negative (downward) force distribution over the entirety of its span; see Fig. 13. However counterintuitive it may seem, this solution is optimal: the overall lift distribution (i.e., when considering the lift contribution from all surfaces, including those of the tail), is indeed very close to elliptical.

To investigate whether the download on the strut is due to a lack of geometric flexibility, the same optimization problem was repeated, but with the twist of the strut allowed to vary. The new solution (not shown here) remained almost identical. This intriguing result may be explained by the transonic and compressible nature of the flow. Indeed, it was found by Ko et al. [62] that the wing-strut opening effectively acts as a nozzle, choking the flow at the minimum area

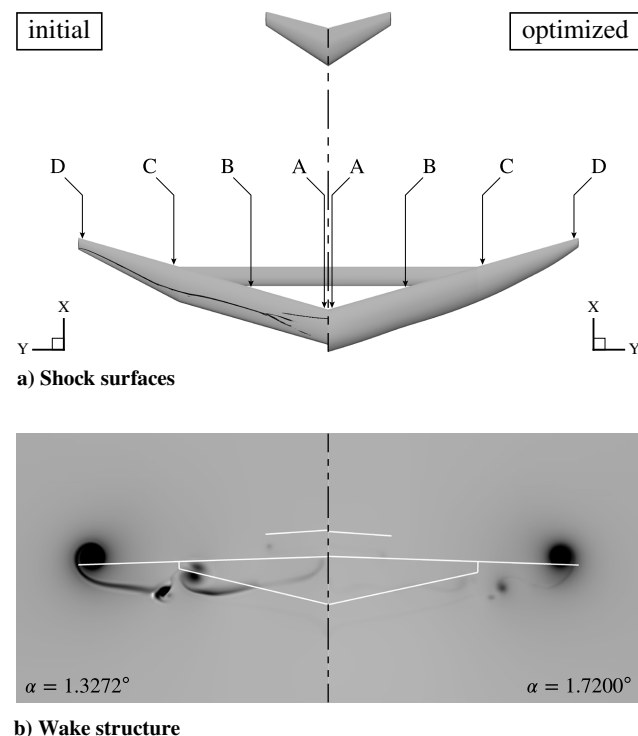


Fig. 12 Initial (left) and optimized (right) braced-wing configurations.

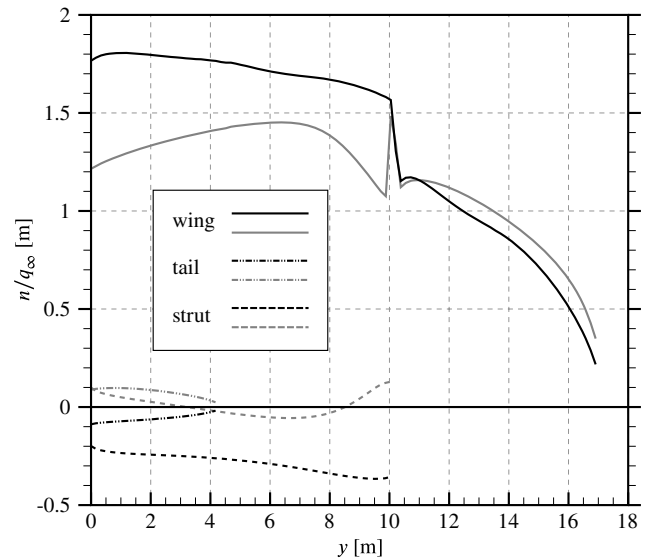


Fig. 13 Initial (gray) and optimized (black) normal-force distributions of the braced-wing configuration.

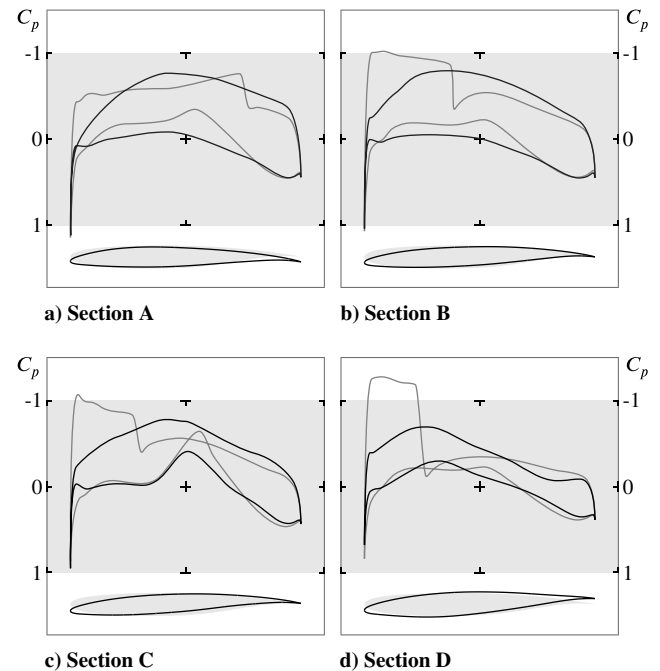


Fig. 14 Initial (gray) and optimized (black) pressure-coefficient profiles of the braced-wing configuration. Sections A–D correspond to those of Fig. 12a.

between the top surface of the strut and the bottom surface of the wing. Having nowhere else to go, the flow spills under the strut at higher velocities, and thus lower pressures, thereby creating the downward force. Here, the optimizer mitigated this nozzle effect by increasing the vertical extent of the strut as much as it could, i.e., by maximizing the nozzle area.

It is worth noting that the downward force on the strut acted in favor of the trim constraint. Consequently, the optimizer did not contort the wing sections at the root as it did for the tube and wing. Still, as seen in Fig. 14, the final wing sections are substantially different from the initial ones.

IV. Conclusions

This paper presented the Euler-equation-based drag minimization of four distinct unconventional aircraft configurations targeted at the regional market segment. The same gradient-based optimization

framework was used in each case in order to enable direct comparisons based on inviscid pressure drag. Relative to the baseline tube and wing, it was found that the box-wing, C-tip blended-wing-body, and braced-wing configurations investigated here produced, respectively, 34.1, 36.2, and 40.3% less induced drag.

The optimization results reinforced the realization that higher-fidelity models than normally used are required for the investigation and assessment of unconventional aircraft configurations. Here, the Euler equations proved to be accurate enough to not only capture but also exploit the nonlinear flow features of each configuration.

For the tube and wing, the optimizer morphed a winglet out of a planar wingtip extension without user intervention. It also applied significant side forces to the winglet, in agreement with previous work [57] stating that such forces are essential for diffusing the vortex at the tip. The final spanwise lift distribution is smooth and close to elliptical despite the side forces experienced by the winglet and the small negative lift carried by the tail to trim the aircraft.

For the box wing, the optimizer reoriented the freestream angle of attack toward the out-of-plane axis of the front and rear wings, thus increasing their effective height-to-span ratio and span efficiency. It also adjusted the optimal force distribution to meet the trim constraint without any apparent drag penalty. This unique capability of the box-wing configuration to satisfy trim, stability, and possibly other requirements without penalizing induced drag largely compensates for its slight underperformance relative to other unconventional configurations of larger span such as the blended-wing-body and braced-wing configurations considered in this study.

For the blended wing-body, the optimizer shrunk the horizontal segment of the C-tip extension as much as it could, suggesting that, when compressibility effects are accounted for, a C tip is not advantageous over a vertical winglet of the same height. Since compressibility effects reduce with increasing winglet height, it may be that this conclusion is unique to the configuration considered here.

For the braced wing, the optimizer easily satisfied the lift and trim constraints through minor twist and section shape changes. It also opted to generate a downward force on the strut in order to mitigate the nozzle effect in the wing-strut opening. However, by compensating with more lift on the wing, it still achieved an almost perfect overall elliptical lift distribution.

This study provides a unique perspective on the influence of flow nonlinearity on induced drag and the related implications for unconventional aircraft design. It does not, however, provide a definitive answer as to which unconventional aircraft is most promising. To help answer such questions, it is imperative to also include the effects of viscosity and structures, among others, within the optimization problem. Such optimizations will be the focus of future research.

Acknowledgments

The authors are grateful for the financial support provided by the Governments of Quebec and Ontario, as well as the University of Toronto. Computations were performed on the General Purpose Cluster supercomputer of the SciNet High Performance Computing Consortium.

References

- [1] Green, J. E., "Civil Aviation and the Environment—The Next Frontier for the Aerodynamicist," *Aeronautical Journal*, Vol. 110, No. 1110, 2006, pp. 469–486.
- [2] Bushnell, D. M., "Frontier Aerospace Opportunities," NASA TR-TM-2014-218519, 2014.
- [3] Kroo, I., "Nonplanar Wing Concepts for Increased Aircraft Efficiency," *Innovative Configurations and Advanced Concepts for Future Civil Transport Aircraft*, VKI Lecture Series, edited by Torenbeek, E., and Deconinck, H., von Kármán Inst., Sint-Genesius-Rode, Belgium, 2005.
- [4] Munk, M. M., "The Minimum Induced Drag of Aerofoils," NACA TR-121, 1923.
- [5] Prandtl, L., "Induced Drag of Multiplanes," NACA TR-TN-182, 1924.
- [6] Cone, C. D., "The Theory of Induced Lift and Minimum Induced Drag of Nonplanar Lifting Systems," NASA TR-R-139, 1962.
- [7] Blackwell, J. A., "Numerical Method to Calculate the Induced Drag or Optimum Loading for Arbitrary Non-Planar Aircraft," NASA TR-SP-405, 1976.
- [8] Verstraeten, J. G., and Slingerland, R., "Drag Characteristics for Optimally Span-Loaded Planar, Wingletted, and C Wings," *Journal of Aircraft*, Vol. 46, No. 3, 2009, pp. 962–971. doi:10.2514/1.39426.
- [9] Ning, S. A., and Kroo, I., "Multidisciplinary Considerations in the Design of Wings and Wing Tip Devices," *Journal of Aircraft*, Vol. 47, No. 2, 2010, pp. 534–543. doi:10.2514/1.41833.
- [10] Jansen, P. W., Perez, R. E., and Martins, J. R. R. A., "Aerostructural Optimization of Nonplanar Lifting Surfaces," *Journal of Aircraft*, Vol. 47, No. 5, 2010, pp. 1490–1503. doi:10.2514/1.44727.
- [11] Andrejašič, M., and Veble, G., "Shape Optimization of Nonplanar Lifting Surfaces and Planar-Nonplanar Break Points," *Journal of Aircraft*, Vol. 50, No. 3, 2013, pp. 798–806. doi:10.2514/1.C031991.
- [12] Nguyen, N., Trinh, K., Reynolds, K., Kless, J., Aftosmis, M., Urnes, J., and Ippolito, C., "Elastically Shaped Wing Optimization and Aircraft Concept for Improved Cruise Efficiency," *51st AIAA Aerospace Sciences Meeting Including the New Horizons Forum and Aerospace Exposition*, AIAA Paper 2013-0141, 2013. doi:10.2514/6.2013-141.
- [13] van Dam, C. P., "Induced-Drag Characteristics of Crescent-Moon-Shaped Wings," *Journal of Aircraft*, Vol. 24, No. 2, 1987, pp. 115–119. doi:10.2514/3.45427.
- [14] Smith, S. C., "A Computational and Experimental Study of Nonlinear Aspects of Induced Drag," NASA TR-TP-3598, 1996.
- [15] Smith, S. C., and Kroo, I. M., "Induced Drag Computations on Wings with Accurately Modeled Wakes," *Journal of Aircraft*, Vol. 34, No. 2, 1997, pp. 253–255. doi:10.2514/2.7570.
- [16] Liersch, C. M., Streit, T., and Visser, K. D., "Numerical Implications of Spanwise Camber on Minimum Induced Drag Configurations," *47th AIAA Aerospace Sciences Meeting Including The New Horizons Forum and Aerospace Exposition*, AIAA Paper 2009-0898, 2009. doi:10.2514/6.2009-898.
- [17] Werner-Westphal, C., Heinze, W., and Horst, P., "Multidisciplinary Integrated Preliminary Design Applied to Unconventional Aircraft Configurations," *Journal of Aircraft*, Vol. 45, No. 2, 2008, pp. 581–590. doi:10.2514/1.32138.
- [18] LaRocca, G., and van Tooren, M. J. L., "Knowledge-Based Engineering Approach to Support Aircraft Multidisciplinary Design and Optimization," *Journal of Aircraft*, Vol. 46, No. 6, 2009, pp. 1875–1885. doi:10.2514/1.39028.
- [19] Seywald, K., Hellmundt, F., Wildschek, A., and Holzapfel, F., "Airworthiness Investigation of a Highly Nonplanar Flexible Wing Concept," *29th Congress of International Council of the Aeronautical Sciences*, ICAS Paper 2014-0088, Bonn, 2014.
- [20] Vassberg, J. C., and Jameson, A., "Theoretical Background for Aerodynamic Shape Optimization," *Introduction to Optimization and Multidisciplinary Design in Aeronautics and Turbomachinery*, edited by Périaux, J., and Verstraete, T., VKI Lecture Series, von Kármán Inst., Sint-Genesius-Rode, Belgium, 2014.
- [21] Makino, Y., Iwamiya, T., and Lei, Z., "Fuselage Shape Optimization of a Wing-Body Configuration with Nacelles," *Journal of Aircraft*, Vol. 40, No. 2, 2003, pp. 297–302. doi:10.2514/2.3093.
- [22] Koc, S., Kim, H.-J., and Nakahashi, K., "Aerodynamic Design of Complex Configurations with Junctions," *Journal of Aircraft*, Vol. 43, No. 6, 2006, pp. 1838–1844. doi:10.2514/1.20723.
- [23] Hicken, J. E., and Zingg, D. W., "Induced-Drag Minimization of Nonplanar Geometries Based on the Euler Equations," *AIAA Journal*, Vol. 48, No. 11, 2010, pp. 2564–2575. doi:10.2514/1.J050379.
- [24] Leung, T. M., and Zingg, D. W., "Aerodynamic Shape Optimization of Wings Using a Parallel Newton-Krylov Approach," *AIAA Journal*, Vol. 50, No. 3, 2012, pp. 540–550. doi:10.2514/1.J051192.
- [25] Schmidt, S., Ilic, C., Schulz, V., and Gauger, N. R., "Three-Dimensional Large-Scale Aerodynamic Shape Optimization Based on Shape Calculus," *AIAA Journal*, Vol. 51, No. 11, 2013, pp. 2615–2627. doi:10.2514/1.J052245.
- [26] Takenaka, K., Hatanaka, K., Yamazaki, W., and Nakahashi, K., "Multidisciplinary Design Exploration for a Winglet," *Journal of*

- Aircraft*, Vol. 45, No. 5, 2008, pp. 1601–1611.
doi:10.2514/1.33031
- [27] Kenway, G. K. W., and Martins, J. R. R. A., “Multipoint High-Fidelity Aerostructural Optimization of a Transport Aircraft Configuration,” *Journal of Aircraft*, Vol. 51, No. 1, 2014, pp. 144–160.
doi:10.2514/1.C032150.
 - [28] Khosravi, S., and Zingg, D. W., “A Numerical Optimization Study on Winglets,” *15th AIAA/ISSMO Multidisciplinary Analysis and Optimization Conference*, AIAA Paper 2014-2173, 2014.
doi:10.2514/6.2014-2173.
 - [29] Lange, R. H., “Review of Unconventional Aircraft Design Concepts,” *Journal of Aircraft*, Vol. 25, No. 5, 1988, pp. 385–392.
doi:10.2514/3.45592.
 - [30] Drela, M., “Development of the D8 Transport Configuration,” *29th AIAA Applied Aerodynamics Conference*, AIAA Paper 2011-3970, 2011.
doi:10.2514/6.2011-3970.
 - [31] Whitcomb, R. T., “Review of NASA Supercritical Airfoils,” *9th Congress of the International Council of the Aeronautical Sciences*, ICAS, Haifa, Israel, 1974.
 - [32] Gagnon, H., and Zingg, D. W., “Geometry Generation of Complex Unconventional Aircraft with Application to High-Fidelity Aerodynamic Shape Optimization,” *21st AIAA Computational Fluid Dynamics Conference*, AIAA Paper 2013-2850, 2013.
doi:10.2514/6.2013-2850.
 - [33] Raymer, D. P., *Aircraft Design: A Conceptual Approach*, 5th ed., AIAA Education Series, AIAA, Reston, VA, 2012.
 - [34] Lange, R. H., Cahill, J. F., Bradley, E. S., Eudaily, R. R., Jenness, C. M., and MacWilkinson, D. G., “Feasibility Study of the Transonic Biplane Concept for Transport Aircraft Application,” NASA Rept. NASA-CR-132462, 1974.
 - [35] Frediani, A., “The Prandtl Wing,” *Innovative Configurations and Advanced Concepts for Future Civil Transport Aircraft*, VKI Lecture Series, edited by Torenbeek, E., and Deconinck, H., von Kármán Inst., Sint-Genesius-Rode, Belgium, 2005.
 - [36] Addoms, R. B., and Spaid, F. W., “Aerodynamic Design of High-Performance Biplane Wings,” *Journal of Aircraft*, Vol. 12, No. 8, 1975, pp. 629–630.
doi:10.2514/3.59846
 - [37] Qin, N., Vavalle, A., Le Moigne, A., Laban, M., Hackett, K., and Weierfellt, P., “Aerodynamic Considerations of Blended Wing Body Aircraft,” *Progress in Aerospace Sciences*, Vol. 40, No. 6, 2004, pp. 321–343.
doi:10.1016/j.paerosci.2004.08.001
 - [38] Peigin, S., and Epstein, B., “Computational Fluid Dynamics Driven Optimization of Blended-Wing-Body Aircraft,” *AIAA Journal*, Vol. 44, No. 11, 2006, pp. 2736–2745.
doi:10.2514/1.19757.
 - [39] Hileman, J. I., Spakovszky, Z., Drela, M., Sargeant, M. A., and Jones, A., “Airframe Design for Silent Fuel-Efficient Aircraft,” *Journal of Aircraft*, Vol. 47, No. 3, 2010, pp. 956–969.
doi:10.2514/1.46545
 - [40] Lyu, Z., and Martins, J. R. R. A., “Aerodynamic Design Optimization Studies of a Blended-Wing-Body Aircraft,” *Journal of Aircraft*, Vol. 51, No. 5, 2014, pp. 1604–1617.
doi:10.2514/1.C032491
 - [41] Reist, T. A., and Zingg, D. W., “Optimization of the Aerodynamic Performance of Regional and Wide-Body-Class Blended Wing-Body Aircraft,” *33rd AIAA Applied Aerodynamics Conference*, AIAA Paper 2015-3292, 2015.
doi:10.2514/6.2015-3292
 - [42] McMasters, J. H., and Kroo, I. M., “Advanced Configurations for Very Large Transport Airplanes,” *Aircraft Design*, Vol. 1, No. 4, 1998, pp. 217–242.
doi:10.1016/S1369-8869(98)00018-4
 - [43] Liebeck, R. H., “Design of the Blended-Wing-Body Subsonic Transport,” *Journal of Aircraft*, Vol. 41, No. 1, 2004, pp. 10–25.
doi:10.2514/1.9084
 - [44] Pfenninger, W., “Design Considerations of Large Global Range High Subsonic Speed LFC Transport Airplanes,” AGARD TR-R-654, Neuilly-sur-Seine, France, 1977.
 - [45] Gundlach, J. F., Tétrault, P.-A., Gern, F. H., Nagshineh-Pour, A. H., Ko, A., Schetz, J. A., Mason, W. H., Kapania, R. K., Grossman, B., and Haftka, R. T., “Conceptual Design Studies of a Strut-Braced Wing Transonic Transport,” *Journal of Aircraft*, Vol. 37, No. 6, 2000, pp. 976–983.
doi:10.2514/2.2724
 - [46] Gern, F. H., Nagshineh-Pour, A. H., Sulaeman, E., Kapania, R. K., and Haftka, R. T., “Structural Wing Sizing for Multidisciplinary Design Optimization of a Strut-Braced Wing,” *Journal of Aircraft*, Vol. 38, No. 1, 2001, pp. 154–163.
doi:10.2514/2.2747
 - [47] Gur, O., Schetz, J. A., and Mason, W. H., “Aerodynamic Considerations in the Design of Truss-Braced-Wing Aircraft,” *Journal of Aircraft*, Vol. 48, No. 3, 2011, pp. 919–939.
doi:10.2514/1.C031171
 - [48] Bhatia, M., Kapania, R. K., and Haftka, R. T., “Structural and Aeroelastic Characteristics of Truss-Braced Wings: A Parametric Study,” *Journal of Aircraft*, Vol. 49, No. 1, 2012, pp. 302–310.
doi:10.2514/1.C031556
 - [49] Bradley, M. K., and Droney, C. K., “Subsonic Ultra Green Aircraft Research Phase II: $N + 4$ Advanced Concept Development,” NASA TR-CR-2012-217556, 2012.
 - [50] Carrier, G., Atinault, O., Dequand, S., Hantrais-Gervois, J.-L., Liauzun, C., Paluch, B., Rodde, A.-M., and Toussaint, C., “Investigation of a Strut-Braced Wing Configuration for Future Commercial Transport,” *28th Congress of the International Council of the Aeronautical Sciences*, ICAS Paper 2012-1.10.2, Bonn, 2012.
 - [51] Hicken, J. E., and Zingg, D. W., “Aerodynamic Optimization Algorithm with Integrated Geometry Parameterization and Mesh Movement,” *AIAA Journal*, Vol. 48, No. 2, 2010, pp. 400–413.
doi:10.2514/1.44033
 - [52] Gagnon, H., and Zingg, D. W., “Two-Level Free-Form and Axial Deformation for Exploratory Aerodynamic Shape Optimization,” *AIAA Journal*, Vol. 53, No. 7, 2015, pp. 2015–2026.
doi:10.2514/1.J053575
 - [53] van Dam, C. P., Nikfetrat, K., Wong, K., and Vijgen, P. M. H. W., “Drag Prediction at Subsonic and Transonic Speeds Using Euler Methods,” *Journal of Aircraft*, Vol. 32, No. 4, 1995, pp. 839–845.
doi:10.2514/3.46799
 - [54] Yamazaki, W., Matsushima, K., and Nakahashi, K., “Aerodynamic Design Optimization Using the Drag-Decomposition Method,” *AIAA Journal*, Vol. 46, No. 5, 2008, pp. 1096–1106.
doi:10.2514/1.30342
 - [55] Chernukhin, O., and Zingg, D. W., “Multimodality and Global Optimization in Aerodynamic Design,” *AIAA Journal*, Vol. 51, No. 6, 2013, pp. 1342–1354.
doi:10.2514/1.J051835
 - [56] Osunizy, L., Buckley, H., Reist, T., and Zingg, D. W., “Drag Minimization Based on the Navier–Stokes Equations Using a Newton-Krylov Approach,” *AIAA Journal*, Vol. 53, No. 6, 2015, pp. 1555–1577.
doi:10.2514/1.J053457
 - [57] Whitcomb, R. T., “A Design Approach and Selected Wind-Tunnel Results at High Subsonic Speeds for Wing-Tip Mounted Winglets,” NASA TR-TN-D-8260, 1976.
 - [58] Gagnon, H., and Zingg, D. W., “Aerodynamic Optimization Trade Study of a Box-Wing Aircraft Configuration,” AIAA Paper 2015-0695, 2015.
 - [59] Wolkovitch, J., “The Joined Wing: An Overview,” *Journal of Aircraft*, Vol. 23, No. 3, 1986, pp. 161–178.
doi:10.2514/3.45285
 - [60] Cerón-Muñoz, H. D., Diaz-Izquierdo, D. O., Solarte-Pineda, J., and Catalano, F. M., “Aerodynamic Interference of Wingtip and Wing Devices on BWB Model,” *29th Congress of International Council of the Aeronautical Sciences*, ICAS Paper 2014-0933, Bonn, 2014.
 - [61] Demasi, L., Dipace, A., Monegato, G., and Cavallaro, R., “Invariant Formulation for the Minimum Induced Drag Conditions of Nonplanar Wing Systems,” *AIAA Journal*, Vol. 52, No. 10, 2014, pp. 2223–2240.
doi:10.2514/1.J052837
 - [62] Ko, A., Mason, W. H., and Grossman, B., “Transonic Aerodynamics of a Wing/Pylon/Strut Junction,” *21st AIAA Applied Aerodynamics Conference*, AIAA Paper 2003-4062, 2003.
doi:10.2514/6.2003-4062